Distinct cytosolic complexes containing the type III secretion system ATPase resolved by 3D single-molecule tracking in live *Yersinia enterocolitica*

Joshua R Prindle[a], Yibo Wang[a], Julian Rocha[a], Andreas Diepold[b], Andreas Gahlmann[a,c,#]

[a]Department of Chemistry, University of Virginia, Charlottesville, Virginia, USA
[b]Max Planck Institute for Terrestrial Microbiology, Marburg, Germany
[c]Department of Molecular Physiology & Biological Physics, University of Virginia School of Medicine, Charlottesville, Virginia, USA

#Address correspondence to Andreas Gahlmann, agahlmann@virginia.edu

Abstract

The membrane-embedded injectisome, the structural component of the virulence-associated type III secretion system (T3SS), is used by gram-negative bacterial pathogens to inject species-specific effector proteins into eukaryotic host cells. The cytosolic injectisome proteins are required for export of effectors and display both stationary, injectisome-bound populations as well as freely-diffusing cytosolic populations. How the cytosolic injectisome proteins interact with each other in the cytosol and associate with membrane-embedded injectisomes remains unclear. Here, we utilize 3D single-molecule tracking to resolve distinct cytosolic complexes of injectisome proteins in living *Yersinia enterocolitica* cells. Tracking of the eYFP-labeled ATPase, *Ye*SctN, and its regulator, *Ye*SctL, reveals that these proteins form a cytosolic complex with each other and then further with *Ye*SctQ. *Ye*SctNL and *Ye*SctNLQ complexes can be observed both in wild type cells and in Δ*sctD* mutants, which cannot assemble injectisomes. In Δ*sctQ* mutants, the relative abundance of the *Ye*SctNL complex is considerably increased. These data indicate that distinct cytosolic complexes of injectisome proteins can form prior to injectisome binding, which has important implications for how injectisomes are functionally regulated.

Importance

Injectisomes are membrane-embedded, multiprotein assemblies used by bacterial pathogens to inject virulent effector proteins into eukaryotic host cells. Protein secretion is regulated by cytosolic proteins that dynamically bind and unbind at injectisomes. However, how these regulatory proteins interact with each other remains unknown. By measuring the diffusion rates of single molecules in living cells, we show that cytosolic injectisome proteins form distinct oligomeric complexes with each other prior to binding to injectisomes. We additionally identify the molecular compositions of these complexes and quantify their relative abundances. Quantifying to what extent cytosolic proteins exist as part of larger complexes in living cells has important implications for deciphering the complexity of biomolecular mechanisms. The results and methods reported here are thus relevant for advancing our understanding of how injectisomes, and related multiprotein assemblies, such as bacterial flagellar motors, are functionally regulated.

INTRODUCTION

Bacterial type III secretion systems (T3SS) are used by gram-negative bacteria to assemble flagellar motors for cell motility and injectisomes that translocate virulence factors, called effector proteins, into eukaryotic host cells. Injectisomes are expressed by many bacterial pathogens, including *E. coli, Salmonella, Pseudomonas, Shigella,* and *Yersinia,* which are responsible for widespread human disease both historically and currently . Flagellar motors and injectisomes are large, multicomponent protein structures that span two and sometimes three cell membranes, as well as the bacterial cell wall (1). Assembly of the injectisome is achieved through hierarchal secretion of early, intermediate, and late secretion substrates (1–7). Early secretion substrates form an extracellular needle that extends away from the bacterial cell envelope. Upon contact with a host cell, middle secretion substrates are secreted through the needle to form a translocon pore in the eukaryotic cell membrane (1–4). Late secretion substrates, also called effector proteins, are then translocated into the host cell cytosol (5–7). While there are species-specific differences among the effector proteins, the structural proteins of injectisomes are highly conserved (8).

Molecular-resolution structures of the fully-assembled cytosolic injectisome complex remain elusive. The cytosolic injectisome proteins SctN, L, Q, and K, associate with the injectisome loosely and transiently, so that structural imaging of fully-assembled injectisomes is only possible *in situ* through the use of cryo-electron tomography (cryo-ET) (9–13). Injectisomes in *Salmonella* and *Shigella* minicell mutants were found to not exhibit continuous densities representative of a cytosolic ring (C-ring) (9, 10), a feature that has been observed consistently for bacterial flagellar motors (3, 14). Instead, the sub-tomogram averages suggested six distinct pods composed of SctK, Q, and L that seem to cradle the hexameric ATPase (9, 10). More recently, cryo-focused ion beam milling followed by cryo-ET enabled the visualization of *Y. enterocolitica* injectisomes inside the phagosomes of infected human myeloid cells (15). In contrast to the six distinct cytosolic pods observed in *Shigella* and *Salmonella* minicell mutants, the *Y. enterocolitica* injectisome contained more continuous, ring-like densities likely composed of SctD, K, and Q, and a 6-fold symmetric, cradle-like structure likely composed of SctL.

The cytosolic injectisome proteins have substantial freely-diffusing populations. *In vivo* fluorescence recovery after photobleaching (FRAP) experiments revealed a continual exchange (on a 1-minute time scale) between freely-diffusing and injectisome-bound states for *Ye*SctQ (*Ye* prefix indicates *Yersinia enterocolitica*). Interestingly, the *Ye*SctQ exchange rate at the injectisome increased by a factor of two upon chemical activation of secretion (16), suggesting that structural dynamism may be important for functional regulation of type 3 secretion. Fluorescence correlation spectroscopy (FCS) further revealed the presence of freely-diffusing and injectisome-bound populations for *Ye*SctK, L, and N (17). In that study, the *average* diffusion rate for each cytosolic injectisome protein shifted upon chemical activation of secretion. These results further point to a dynamic and adaptive network of cytosolic interactions that may be required for injectisome binding. Earlier work from our lab identified two distinct *Ye*SctQ-containing cytosolic protein complexes in living cells (18). However, the full compositions of these and additional SctQ-independent cytosolic complexes are yet to be determined.

Efforts at reconstituting cytosolic injectisome protein complexes *in vitro* have begun to elucidate how these proteins may interact with one another. Native mass spectrometry (MS) experiments showed the ability of *Se*SctQ (*Se* prefix indicates *Salmonella enterica*) to bind *Se*SctL and N with various stoichiometries. Importantly however, a *Se*SctL$_2$:*Se*SctN heterotrimer was consistently observed in any complex that included these two proteins (19). Dynamic light scattering was used to determine the relative size of cytosolic injectisome proteins and their respective complexes (20). Key differences were observed for reconstituted complexes containing *Sf*SctK and *Sf*SctQ and complexes containing *Sf*SctQ and *Sf*SctL (*Sf* prefix indicates *Shigella flexneri*). Specifically, the complex of *Sf*SctK and *Sf*SctQ is globular and compact (hydrodynamic diameter = 10.2 nm), whereas the complex of *Sf*SctQ and *Sf*SctL is much larger (hydrodynamic diameter = 18.5 nm). These differences were attributed to the ability of *Sf*SctQ to adopt different conformational states depending on its binding partner.

To gain further insights into how the cytosolic injectisome protein complexes interact with each other in living *Y. enterocolitica*, we use 3D single-molecule localization and tracking microscopy to resolve the different diffusive states of *Ye*SctQ, L, and N in different genetic backgrounds. We show that deletion

of the injectisome protein *Ye*SctD, which presumably binds *Ye*SctK(15), abrogates the clustered, membrane proximal localization of all cytosolic injectisome proteins and increases the abundance of the same cytosolic complexes that are also present in wild-type cells. We further find that deletion of *Ye*SctQ increases the abundance of a complex containing *Ye*SctN and L and eliminates the diffusive state assigned to the larger complex containing *Ye*SctN, L, and Q. Comparing the diffusion rates of all tracked proteins allows us to distinguish between oligomerization models that differ in terms of protein complex stoichiometry. Our combined results narrow down the possible stoichiometries of cytosolic injectisome protein complexes that can form prior to injectisome binding.

RESULTS

Diffusion of monomeric eYFP under secretion-active conditions

Tracking of the cytosolic injectisome proteins under secretion-active conditions requires that cells are exposed to a 25°→37° C temperature jump and that calcium ions are removed from the growth medium through chelation (21–25). Concurrent with the removal of Ca^{2+} ions, $MgCl_2$ and glycerol are added (see methods). The altered growth medium composition results in a different osmotic environment for the cells, which could alter the density of the cytosol. To quantify this effect, we tracked monomeric eYFP under secretion-active conditions in living *Y. enterocolitica* cells. The pooled single-molecule trajectories provide highly sampled distributions of molecular motion behaviors, quantified using the apparent diffusion coefficient (D^*). A simulated library of D^* distributions (**Fig. 1a**) enables linear fitting of experimentally acquired D^* distributions to obtain spectra of intracellular Brownian diffusion coefficients that manifest for a given protein. Peaks in these spectra can be analyzed to determine the diffusion rates of different diffusive states, and the areas underneath the peaks determine their relative abundances. These parameters can then be further refined by nonlinear fitting of a defined number of diffusive states (see Methods). Transforming the raw data (cumulative distribution functions (CDFs) of apparent diffusion coefficients) into diffusion

coefficient spectra addresses a key challenge in analyzing single-molecule tracking data, namely choosing a suitable fitting model among many with different numbers of parameters (diffusive states and their relative abundances) (26, 27).

For monomeric eYFP under secretion-active conditions, we observe a diffusion coefficient spectrum exhibiting a single, well-defined peak at D = 9.1 μm^2/s that produces a good fit to the experimentally acquired D^* distribution (**Fig. 1bc**). Non-linear fitting using a single diffusive state at D = 9.2 μm^2/s results in an equally good fit (**Fig. 1bc**). The narrowness of the sole spectral peak shows that the motion of eYFP is homogeneous in the *Y. enterocolitica* cytosol and well described by a single diffusive state with a Brownian diffusion coefficient at 9.2 μm^2/s. This property establishes eYFP as a suitable probe for measuring the diffusion coefficients for eYFP-labeled proteins. We note that a D = 9.2 μm^2/s diffusive state is slower than the single diffusive state at 11.9 μm^2/s, which we measured previously under standard, i.e. non-secreting, growth conditions (18, 28). This observation is consistent with an overall osmotic upshift that increases the biomolecular density of the cytosol and thus limits the mobility of eYFP. Controlled osmotic upshifts have been previously shown to slow diffusion of fluorescent and fluorescently-labeled proteins (29, 30).

Under secretion-active conditions, we also observe a small (7%) population of slow (D < 0.5 μm^2/s) eYFP, indicating that even small proteins can occasionally get trapped, presumably in crowded pockets of the cytosol (29). We verified that trajectories corresponding to slow moving eYFP are indeed randomly localized to the cytosol and do not show a preference for subcellular locations, such as the membrane or the cell poles (**Supplementary Fig. 1a**). Notably, the slow population is not detectable when tracking eYFP under standard growth conditions.

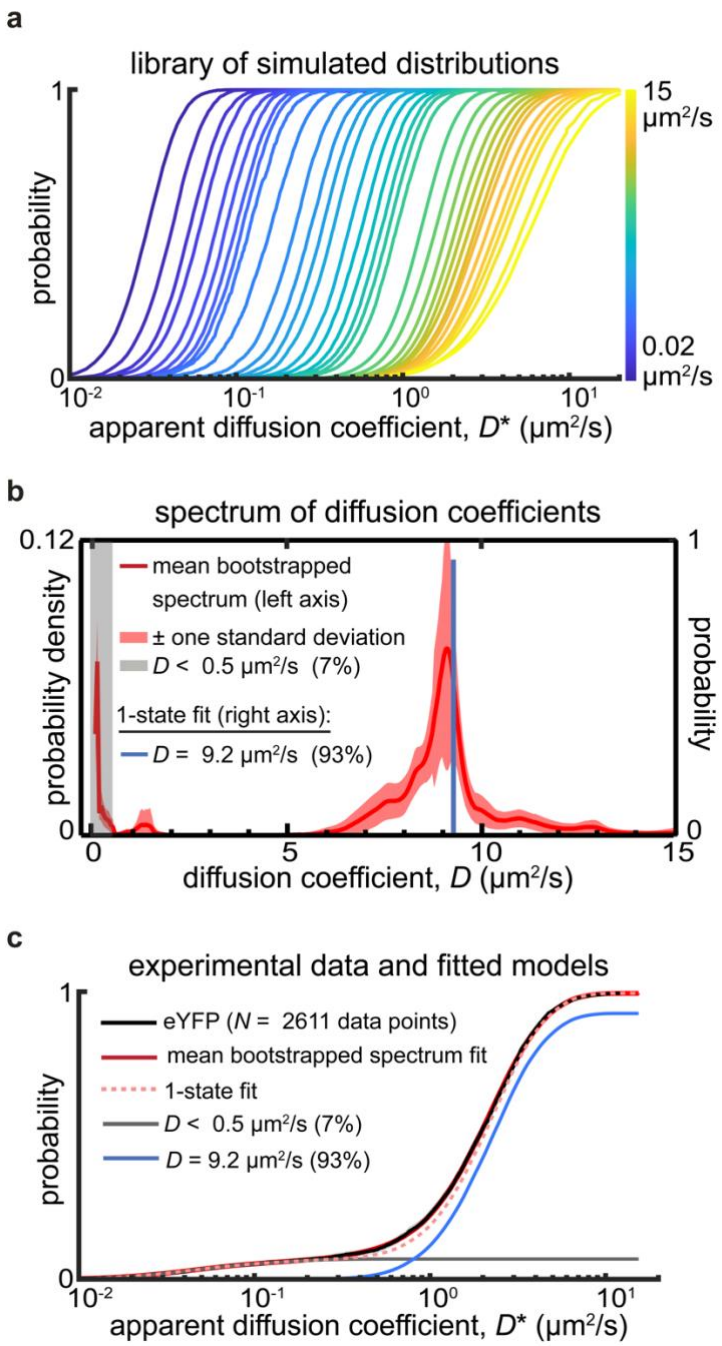

Figure 1: a) Simulated distributions of apparent diffusion coefficients based on Monte Carlo simulations of confined Brownian motion in rod-shaped bacterial cells. These simulations account for both random and systematic measurement errors encountered in single-molecule tracking measurements (see Methods). (**b** and **c**) The experimentally measured apparent diffusion coefficient distribution of freely diffusing eYFP molecules is fit well using a tightly peaked distribution of diffusion coefficients centered at D = 9.2 μm^2/s (red curve in panel b) or using a single diffusive state with D = 9.2 μm^2/s (blue line in panel c). The excellent agreement between theory and experiment supports that the assumption of bacterial cell-confined Brownian diffusion is valid.

Diffusive state assignment of *Ye*SctQ indicates two distinct protein complexes in living cells

Our previously published *Ye*SctQ tracking results in *Y. enterocolitica* under secretion-active conditions suggested the presence of three diffusive states at D ~ 1.0, 4.0, and 15 μm^2/s, with the D ~ 15 μm^2/s diffusive state constituting a 20% population fraction of all tracked proteins. Such a result is however inconsistent with the monomeric eYFP tracking result, as an eYFP-labeled protein should not be able to diffuse faster than 9.2 μm^2/s under secretion-active conditions. We therefore re-examined the raw *Ye*SctQ single-molecule trajectories and found that uncharacteristically fast apparent diffusion coefficients are often due to large displacements resulting from mislocalization of fluorescence signals beyond the axial (z-) boundaries of the cell (**Supplementary Fig. 2**). Removal of these localizations and the associated trajectories removed the fast D = 15 μm^2/s diffusive state. Importantly, the diffusive states below 9.2 μm^2/s are largely unaffected by this filtering step.

In contrast to freely diffusing eYFP (**Fig. 1**), the diffusion coefficient spectrum of *Ye*SctQ shows two prominent peaks at D ~ 1.3 and 4.8 μm^2/s and a small peak at 6.5 μm^2/s in addition to an injectisome-bound, stationary population at D = 0 μm^2/s (**Fig. 2a**). eYFP-*Ye*SctQ fusion proteins were expressed as a genomic replacement under the control of its native promotor in actively secreting cells, and the fusion protein was stable and not degraded (18). These results are roughly consistent with our previous study (18), which identified three cytosolic diffusive states for *Ye*SctQ at D ~ 1.1, 4.0, and 13.9 μm^2/s (the fastest state was assigned to the eYFP-*Ye*SctQ monomer). The distinct peaks in the newly analyzed diffusion coefficient spectrum provide the initial diffusion rates and populations fractions for non-linear fitting of the experimental D^* CDF of *Ye*SctQ. Still, to test whether overfitting the data with too many different diffusive states (i.e. a non-linear model with too many free parameters) could be an issue, we initialized 1-, 2-, and 3-state fits by combining population fractions and initial guesses for diffusion coefficients from the spectrum (see Methods). Non-linear fitting using a 2-state model produced diffusive states at D ~ 1.3, and 5.3 μm^2/s, which agrees with the prominent peaks in the diffusion coefficient spectrum (**Fig. 2a**) although the 5.3 μm^2/s diffusive state appears to be right shifted by the small spectral density at 6.5 μm^2/s. Non-linear fitting using a 3-state model produced diffusive states at D ~ 1.2, 4.4, and 7.0 μm^2/s, however the

population fraction of the $D \sim 7.0$ μm^2/s diffusive state appears to be vastly overestimated (**Supplementary Fig. 5**). Additionally, 5-fold cross-validation analysis favors a 2-state over a 3-state model (**Supplementary Fig. 5**). These results suggest that the majority of *Ye*SctQ is part of two predominant cytosolic complexes diffusing at $D \sim 1.3$ and 4.8 μm^2/s, while the monomeric fraction of this injectisome protein remains small by comparison.

*Ye*SctL shares one diffusive state with *Ye*SctQ

Having reproduced our previously obtained results in the diffusion coefficient spectra, we next analyzed the intracellular diffusive behaviors of eYFP-labeled *Ye*SctL. We had previously tracked *Ye*SctL with PAmCherry1 but chose to switch the fluorescent label to eYFP for the present study due to its homogeneous diffusion behavior in *Y. enterocolitica* (**Fig. 1ab**). Again, we expressed eYFP-*Ye*SctL as a genomic replacement under the control of its native promotor. The eYFP-*Ye*SctL fusion protein was functional and not degraded (**Supplementary Fig. 3 & 4**). Examination of the *Ye*SctL diffusion coefficient spectrum reveals a prominent spectral peak at $D \sim 1.3$ with a small shoulder to the right (**Fig. 2b**). The 3-state model for *Ye*SctL produced diffusive states at $D \sim 1.3$ (population fraction = 17%), 3.2 (population fraction = 3%), and 7.4 μm^2/s (population fraction = 7%). Given that the diffusion coefficient spectrum clearly indicates a prominent peak at $D \sim 1.3$ μm^2/s and does not include a peak at $D \sim 0.9$ or 7.4 μm^2/s, we turned to the 2-state model, whose fitted values agree better with the spectral peak positions. The choice of the 2-state model is also supported by 5-fold cross-validation analysis (**Supplementary Fig. 6**).

The 2-state model provides two diffusive states for *Ye*SctL at $D \sim 1.3$ and 3.1 μm^2/s with corresponding population fractions of 13% and 14%, respectively (**Fig. 2b, Supplementary Fig. 6**). These mobile states are in addition to an abundant (population fraction = 73%) stationary, injectisome-bound population with $D < 0.5$ μm^2/s. Plotting the 3D trajectories using a $D^* = 0.5$ μm^2/s threshold clearly shows membrane-associated clusters representing the injectisome-bound population (**Fig. 2c**). The $D \sim 1.3$ μm^2/s diffusive state is consistent with our previous result obtained with PAmCherry-*Ye*SctL, based on which we

concluded that both *Ye*SctQ and *Ye*SctL diffuse at the same slow rate as part of the same complex (18). The SctLQ interaction is also supported by a number of previous studies (17, 19, 20). On the other hand, the $D \sim 3.1$ μm^2/s *Ye*SctL diffusive state has not been previously observed. The presence of this additional state suggests another homo- or hetero-oligomeric complex containing *Ye*SctL. However, such a complex does not contain *Ye*SctQ, because a $D \sim 3.1$ μm^2/s diffusive state is not observed in the eYFP-*Ye*SctQ data.

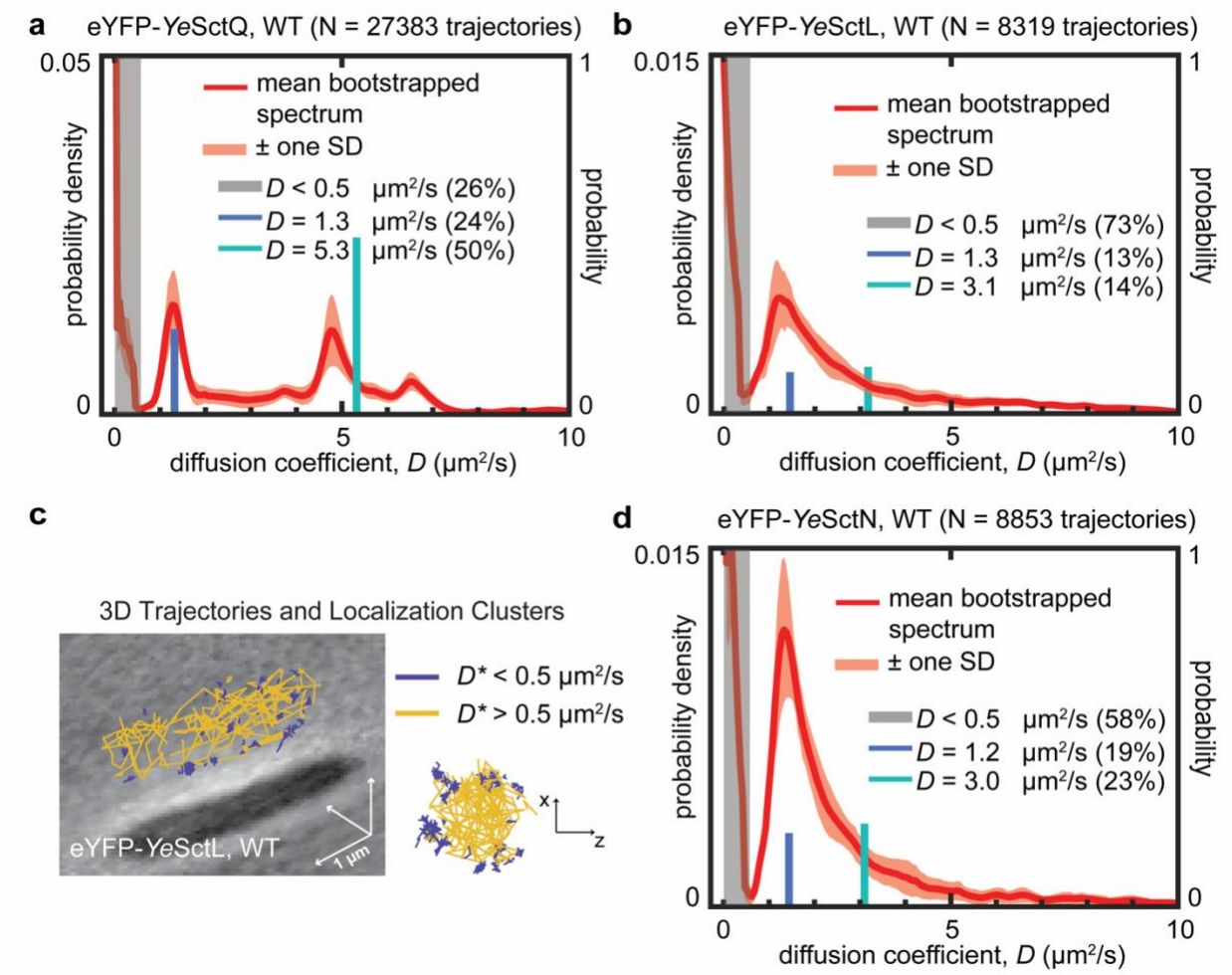

Figure 2: a) Diffusion coefficient spectrum for *Ye*SctQ in wild type cells. The experimentally measured distribution is best fit with two states at $D = 1.3$ μm^2/s and $D \sim 5.3$ μm^2/s (Supplementary Figure 5). b) Diffusion coefficient spectrum for *Ye*SctL in wild type cells. The experimentally measured distribution is best fit with two states at $D = 1.3$ μm^2/s and $D \sim 3.1$ μm^2/s (Supplementary Figure 6). c) 3D trajectories for *Ye*SctL with $D^* < 0.5$ μm^2/s exhibit clustering at the membrane indicative of association with injectisomes. d) Diffusion coefficient spectrum for *Ye*SctN in wild type cells. The experimentally measured distribution is best fit with two diffusive states at $D = 1.2$ μm^2/s and $D \sim 3.0$ μm^2/s (Supplementary Figure 7).

*Ye*SctN and *Ye*SctL share two distinct diffusive states in *Y. enterocolitica*

There are numerous reports documenting interactions between SctN and SctL in both flagellar and virulence-associated T3SSs (31–34). SctL binding prevents SctN hexamerization prior to injectisome binding and thereby negatively regulates SctN's ATPase activity, which is the one of the most well-established functional roles of the cytosolic injectisome proteins (31, 33, 35–38). To detect the SctNL interaction in living cells, we expressed eYFP-*Ye*SctN as a genomic replacement under the control of its native promotor and acquired *Ye*SctN single-molecule trajectories in actively secreting cells. The eYFP-*Ye*SctN fusion protein was functional and only minimally degraded (**Supplementary Fig. 3 & 4**). The resulting diffusion coefficient spectrum shows a very prominent spectral peak at $D \sim 1.3$ μm^2/s with, similar to the *Ye*SctL diffusion coefficient spectrum, a small shoulder to the right (**Fig. 2d**). Non-linear fitting with a 1-state model produces a diffusive state at $D \sim 1.7$ μm^2/s. A 2-state models produces diffusive states at $D \sim 1.2$ and 3.0 μm^2/s with corresponding population fractions of 19% and 23% (**Fig. 2d**, **Supplementary Fig. 7**), a result that better matches the diffusion coefficient spectrum. The 2-state model is also supported by cross-validation analysis (**Supplementary Fig. 7**). The robust emergence of a $D \sim 1.3$ μm^2/s diffusive state, a state that is also observed in YeSctL and YeSctQ measurements (in both the 2- and 3-state models) suggests the formation of a hetero-oligomeric *Ye*SctNLQ complex. The 2-state model produces an intermediate diffusive state at $D \sim 3.0$ μm^2/s, and such a diffusive state was also observed for *Ye*SctL ($D \sim 3.1$ μm^2/s). We thus tentatively assign this diffusive state to a SctNL complex. While the SctNL interaction is supported by a number of previous studies, the population fraction of this state is low for both *Ye*SctN and *Ye*SctL in wild-type cells. We therefore concluded that establishing the existence of this state needed further experimental support.

We argued above that the oligomeric complex that gives rise to the $D \sim 3.0$ μm^2/s diffusive state does not contain *Ye*SctQ. It follows that deletion of *sctQ* should not affect the formation of that complex. To test this hypothesis, we acquired single-molecule trajectories for *Ye*SctN and *Ye*SctL in a Δ*sctQ* mutant background. Remarkably, the CDFs of apparent diffusion coefficients for these two proteins (i.e. the raw data) are essentially congruent in the Δ*sctQ* background, strongly indicating co-diffusive behavior (**Fig. 3a**).

Plotting the 3D trajectories for eYFP-*Ye*SctN in the Δ*sctQ* background using a $D^* = 0.5$ μm^2/s threshold shows an absence of membrane-associated clusters (**Fig. 3b**). The same phenomenon is observed for eYFP-*Ye*SctL in the Δ*sctQ* background (data not shown), indicating that injectisome association is no longer possible in the absence of SctQ (17). The spectra of diffusion coefficients of these two proteins show the same trend: each spectrum contains a prominent peak at $D \sim 2.8$ μm^2/s. Notably, a peak at $D \sim 1.3$ μm^2/s, which we previously assigned to a *Ye*SctNLQ complex, is also absent. A 1-state non-linear fit converged on $D \sim 2.7$ μm^2/s in each case with corresponding population fractions of 93% for *Ye*SctL and 92% for *Ye*SctN, respectively (**Supplementary Fig. 8, Supplementary Fig. 9**).

Together, these results support the conclusion that *Ye*SctL and *Ye*SctN are able to form two distinct cytosolic complexes. One of these complexes contains *Ye*SctQ and the other does not. Under our experimental conditions, the *Ye*SctNLQ complex diffuses at $D \sim 1.3$ μm^2/s, while the *Ye*SctNL complex diffuses at $D \sim 2.8$ μm^2/s. In wild-type cells, the presence of *Ye*SctQ leads to a smaller abundance of the *Ye*SctNL complex in favor of the *Ye*SctNLQ complex as well as injectisome-bound *Ye*SctL and *Ye*SctN.

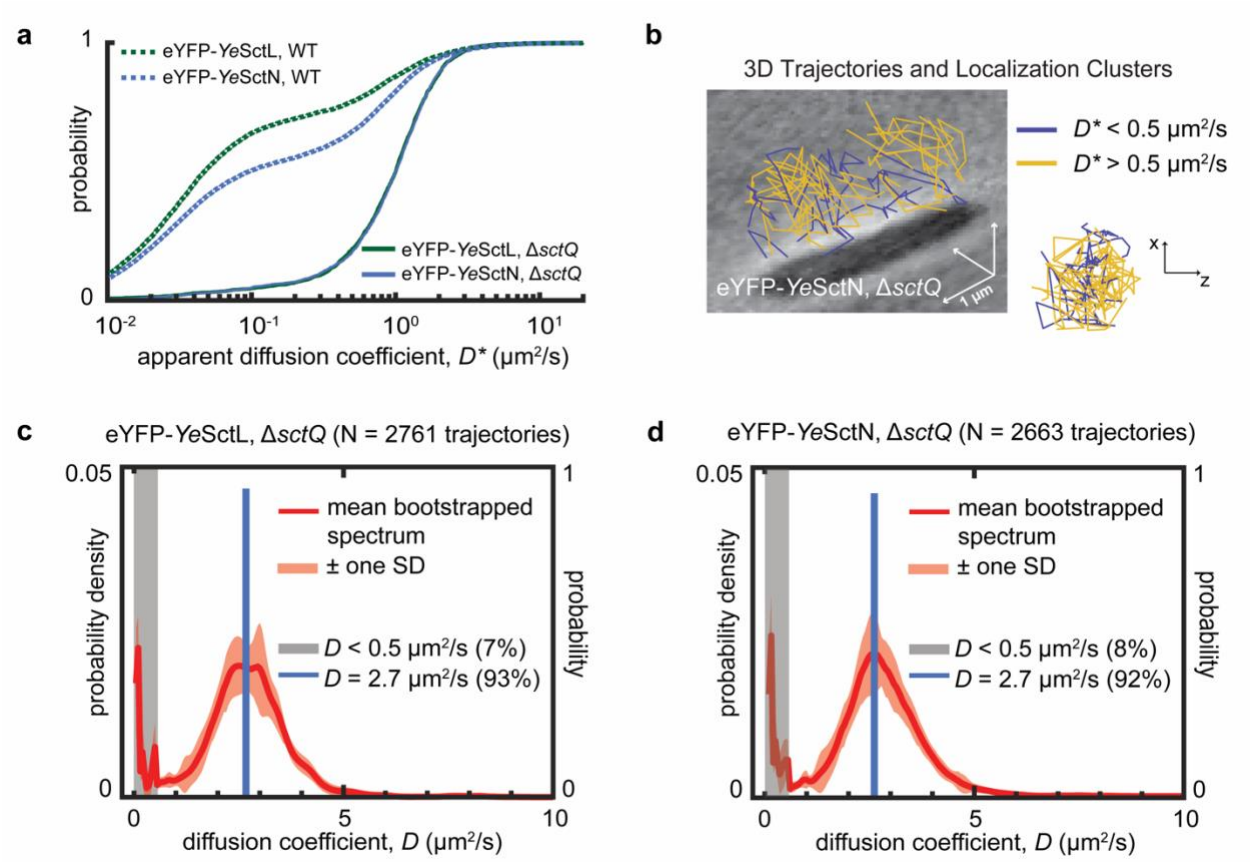

Figure 3: a) Experimentally measured CDFs of *Ye*SctL and *Ye*SctN apparent diffusion coefficients in wild type cells and Δ*sctQ* mutants. The *Ye*SctL and *Ye*SctN distributions overlay very well in the Δ*sctQ* background. b) 3D trajectories for *Ye*SctN in the Δ*sctQ* background show an absence of membrane-associated clusters for $D^* < 0.5$ μm^2/s. c) and d) Diffusion coefficient spectra for *Ye*SctL and *Ye*SctN in the Δ*sctQ* background. In each case, the experimentally measured distribution is best fit with one state at D = 2.7 μm^2/s Supplementary Figure 8 & 9).

Native complex formation among *Ye*SctQ, L, and N increases in the absence of injectisomes

SctD is the inner-membrane ring protein of the injectisome. SctD is required for proper injectisome assembly (39) and subsequent effector protein secretion. SctD provides a binding interface for SctK, which in turn allows SctQ, L, and N to bind to the injectisome (40). Thus, SctQ, L, and N are completely cytosolic in the Δ*sctD* background. To test whether the same diffusive states manifest in the absence of fully-assembled injectisomes, we acquired single-molecule trajectories in the Δ*sctD* mutant background for *Ye*SctQ, L, and N.

The *Ye*SctQ Δ*sctD* spectrum is very similar to the spectrum observed in wild-type cells. Two clear spectral peaks are evident at $D \sim 1.3$, and 4.5 $\mu m^2/s$ (**Fig. 4a, Supplementary Fig. 10**). A 2-state non-linear fit produces diffusive states at $D \sim 1.2$ and 4.5 $\mu m^2/s$, a result that is in excellent agreement with the diffusive state observed in wild-type cells. These data show that the same complexes formed in wild-type cells can also form in the absence of injectisomes. Consistent with the loss of injectisome binding, the combined population fractions of the three distinct cytosolic diffusive states increase. The $D < 0.5$ $\mu m^2/s$ state(s) decreased from 24% in wild-type cells to 10% in the Δ*sctD* mutant. We note however that the 10% of slow diffusing molecules in the Δ*sctD* mutant do not localize to the membrane (**Supplementary Fig. 1b**).

The *Ye*SctL and *Ye*SctN Δ*sctD* spectra both show a broad peak extending from $D \sim 1$ to 4 $\mu m^2/s$. A 2-state fit converges to diffusive states at $D \sim 1.2$ and 2.6 $\mu m^2/s$ for *Ye*SctL and $D \sim 1.0$ and 2.5 $\mu m^2/s$ for *Ye*SctN. Both of these results agree well with the diffusion coefficient spectra (**Fig. 4bc, Supplementary Fig. 11, Supplementary Fig. 12)** and are also in close agreement with the diffusive states observed for each protein in wild-type and Δ*sctQ* cells. Taken together, these results establish that the same complexes formed in wild-type cells can also form, in increased abundance, in the absence of injectisomes. In other words, the presence of injectisomes is not necessary for cytosolic complex formation.

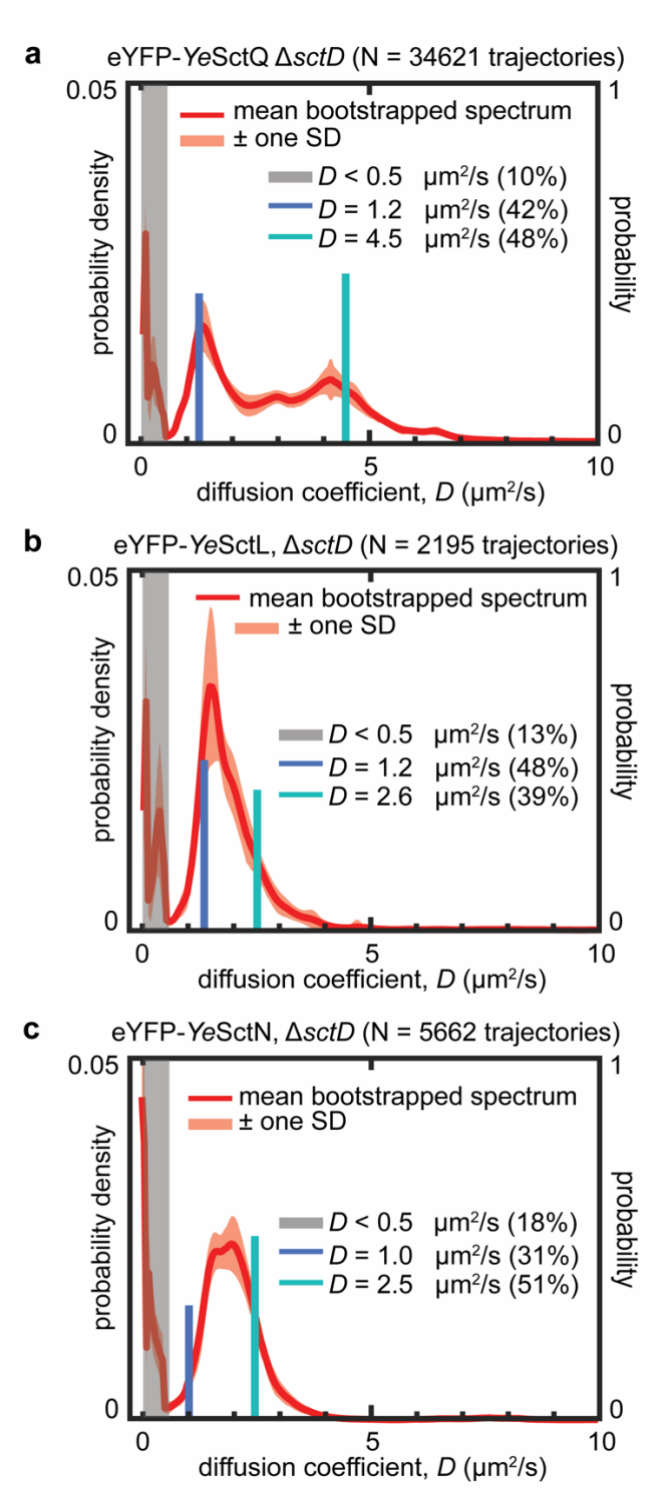

Figure 4: Removal of *Ye*SctD results in an increased abundance of native cytosolic complexes. a) *Ye*SctQ, b) *Ye*SctL, and c) *Ye*SctN all share a diffusive state around $D \sim 1.3$ μm²/s, consistent with results obtained in wild type cells. Also consistent with wild type results is the presence of a diffusive state at $D \sim 4.5$ μm²/s for *Ye*SctQ and the presence of a shared diffusive state for *Ye*SctL and *Ye*SctN at $D \sim 2.5$ μm²/s.

DISCUSSION

Determining the functional role(s) of the cytosolic injectisome proteins has been challenging, because our understanding of their interactions at the injectisome and in the cytosol remains limited. Here, we present live-cell single-molecule tracking data that suggest the formation of distinct, freely-diffusing protein complexes. One complex containing *Ye*SctN and *Ye*SctL, but not *Ye*SctQ, diffuses at $D \sim 2.8$ μm^2/s. A larger complex containing *Ye*SctN, L, and Q diffuses at $D \sim 1.3$ μm^2/s. These complexes form robustly in wild-type and mutant cells that are unable to fully assemble T3SS injectisomes (**Fig. 5a**).

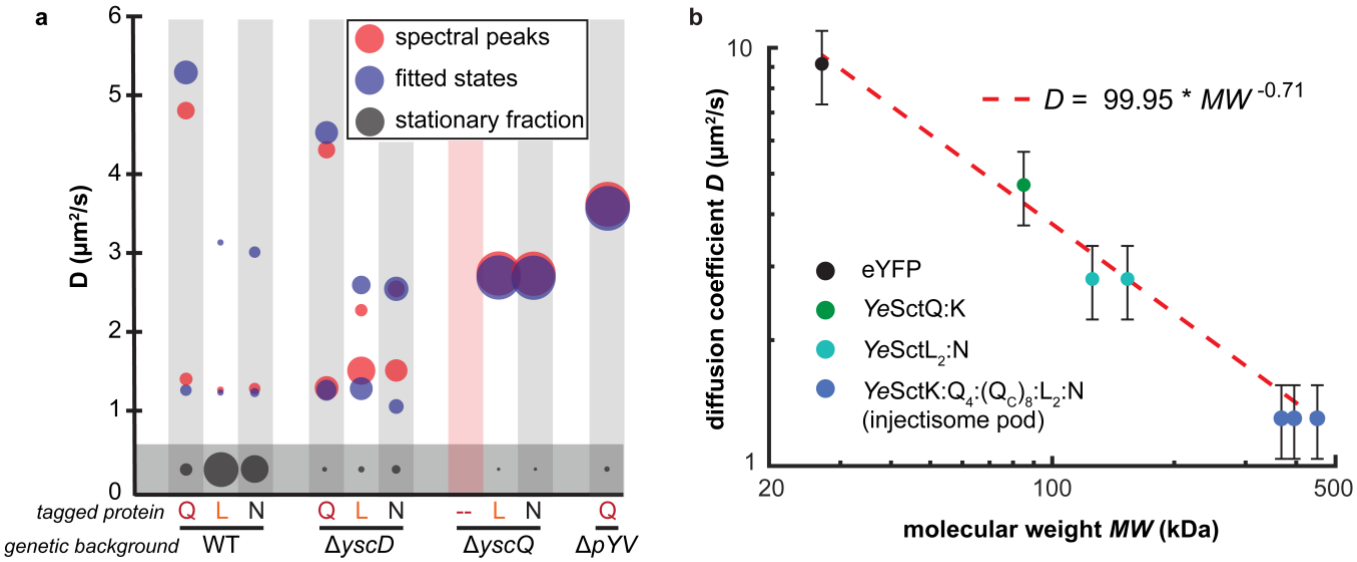

Figure 5: a) Comparison of spectral peaks and fitted diffusive states for each indicated eYFP-labeled injectisome protein tracked in different genetic backgrounds. The relative population fraction for each peak/diffusive state is represented by the size of the circle. Spectra for eYFP-*Ye*SctN and eYFP-*Ye*SctL in the Δ*sctD* mutant do not contain prominent spectral peaks corresponding to the fitted $D \sim 2.8$ μm^2/s diffusive state, whereas prominent spectral peaks are resolved in the Δ*sctQ* mutant. The fitted diffusive states for $D < 0.5$ μm^2/s in the Δ*sctD*, Δ*sctQ*, and Δ*pYV* mutants do not localize to the membrane. b) Measured diffusion coefficients plotted against the molecular weights of the indicated protein complexes. The straight line corresponds to the least squares fit using the model shown.

A *Ye*SctNL complex is consistent with a proposed regulatory mechanism of *Ye*SctL. SctL is thought to negatively regulate ATPase activity in both bacterial flagellar motors and injectisomes by preventing SctN hexamerization in the cytosol(33). Recent cryo-EM data on purified proteins show that the extreme N-terminus of FliI (the flagellar homologue of SctN) contains a charged region to which FliH (the flagellar

homologue of SctL) can bind(41). Abolishing this interaction through point mutations results in a higher propensity of ATPase hexamerization *in vitro*, as well as decreased cell growth and cell motility phenotypes. Further, the SctNL (FliIH) complex has been consistently observed as a heterotrimer using *in vitro* biochemical and biophysical approaches(11, 19, 31, 36, 37, 42, 43), with a dimer of SctL (FliH) binding to the ATPase monomer SctN (FliI). Based on these results, we posit that the $D \sim 2.8$ μm^2/s diffusive state that we observe both wild-type and Δ*sctQ* mutants and the $D \sim 2.5$ μm^2/s diffusive state that we observe in Δ*sctD* mutants is likely due to a *Ye*SctN$_1$:*Ye*SctL$_2$ heterotrimer. In wild-type cells, 19% of *Ye*SctN and 13% of *Ye*SctL contribute to this heterotrimer population. In Δ*sctQ* and Δ*sctD* mutants, the abundance of this heterotrimer increases substantially (93% and 92% for *Ye*SctN and *Ye*SctL, respectively, for Δ*sctQ* and 31% and 48% for *Ye*SctN and *Ye*SctL, respectively, for Δ*sctD*).

A *Ye*SctNLQ complex is consistent with cytosolic pod complexes containing SctN, L, Q, and K. Sub-tomogram averages in *Shigella* and *Salmonella* suggest six distinct pods composed of SctK, Q, and L that seem to cradle the hexameric ATPase at the injectisome(9, 10). Subsequent work has focused on reconstituting such pod complexes *in vitro*. *Se*SctNLQ(19) and *Sf*SctLQK complexes(20) were successfully isolated, and the estimated size and shapes of these complexes were qualitatively consistent with cryo-ET pod densities. Based on these results, we speculate that the $D \sim 1.3$ μm^2/s diffusive state we observe in wild-type cells and in Δ*sctD* mutants is likely not just a SctNLQ complex, but in fact a SctNLQK heterooligomer. This claim is substantiated by the loss of the $D \sim 1.3$ μm^2/s diffusive state when we track eYFP-*Ye*SctL and eYFP-*Ye*SctN proteins in the Δ*sctQ* mutant. Whether a $D \sim 1.3$ μm^2/s diffusive state also manifests for SctK in wild-type cells and in Δ*sctD* mutants remains to be determined.

The molecular composition of the $D \sim 4.8$ μm^2/s diffusive state observed for eYFP-*Ye*SctQ could be consistent with a *Ye*SctQK complex. In our previous work(18), we assigned this intermediate diffusive state to a *Ye*SctQ homo-oligomer that also contains *Ye*SctQ$_C$, the alternatively expressed C-terminal fragment of *Ye*SctQ. This assignment was made based on tracking eYFP-*Ye*SctQ proteins in a Δ*pYV* mutant, which does not express any other T3SS proteins. In that mutant, ~80% of the tracked *Ye*SctQ proteins diffused at $D \sim 3.6$ μm^2/s, which is notably smaller than the $D \sim 4.8$ μm^2/s diffusive state that we observe

in wild type cells. This discrepancy indicates that the $D \sim 3.6$ and 4.8 $\mu m^2/s$ diffusive states likely originate from different complexes. The spectrum of eYFP-*Ye*SctQ diffusion coefficients in a Δ*pYV* background indeed show a prominent spectral peak ranging from $D \sim 3$ to 4.5 $\mu m^2/s$, but little spectral density at $D \sim 4.8$ $\mu m^2/s$ (**Supplementary Fig. 12**). *In vitro* light-scattering measurements on *Sf*SctQ-containing complexes(20) suggested the ability of *Sf*SctQ to adopt different conformational states depending on its interacting partner. A small, globular complex (hydrodynamic diameter = 10.2 nm) was observed upon co-expression and co-purification of *Sf*SctQ and K, while a larger complex (hydrodynamic diameter = 13.4 nm) was observed for co-purified *Sf*SctQ and Q_C. Based on these results, we speculate that the $D \sim 4.8$ $\mu m^2/s$ diffusive state in wild type cells and in Δ*sctD* mutants is due to a *Ye*SctQK complex. In wild-type cells, we observe very little spectral density in the $D = 3.5 - 4$ $\mu m^2/s$ range, which indicates that a *Ye*SctQQ_C complex is not abundantly present. On the other hand, if injectisomes are not assembled, as in the Δ*sctD* mutants, we do observe spectral density in the $D = 3.5 - 4$ $\mu m^2/s$ range. These results indicate that the presence of injectisomes and thus the ability of *Ye*SctQ to bind to and unbind from injectisomes affects the type of complexes that *Ye*SctQ forms in abundance. Determining the compositions and stoichiometries of *Ye*SctQ-containing complexes in specific deletion mutants will be the subject of future work.

Complex formation among cytosolic injectisome proteins may provide the foundation for functional regulation of type 3 secretion. Specifically, a pool of freely diffusing complexes of injectisome proteins that are available for injectisomes binding would provide a mechanism for timely reactivation of secretion. Recent work has shown that an extracellular pH drop from 7 to 4 results in disassociation of *Ye*SctN, L, Q, and K from injectisomes, an effect that correlated with loss of secretion(44). Notably, the intracellular pH decreased only slightly (pH=7→6.3) in acidic extracellular environments. Reverting the external pH from 4 to 7 reverses these effects. Injectisome binding is restored within ~10 min and effector protein secretion resumes shortly thereafter. The results reported here lend further support for a secretion reactivation model relying on cytosolic complexes of injectisome proteins: in Δ*sctQ* and in Δ*sctD* mutants, in which injectisome binding is not possible, we observe clear signatures of the same diffusive states in wild-type cells that we assign to distinct *Ye*SctNLQ, *Ye*SctNL, and *Ye*SctQK complexes.

Identifying which cytosolic injectisome proteins assemble into freely-diffusing complexes in a native biological context can help determine how these proteins bind and unbind dynamically to and from injectisomes. While we have identified the compositions of three prominent complexes, the exact stoichiometries and functions of these complexes remains to be determined. Previous work by others has shown that the cytosolic diffusion rate of proteins scales with molecular weight, but not according to the Stokes-Einstein equation, which stipulates that $D \propto (\text{Molecular Weight})^{-1/3}$. Instead, a $D \propto (\text{Molecular Weight})^{-2/3}$ scaling has been observed by others independently for different proteins(45–48). Here, we obtain a $D \propto (\text{Molecular Weight})^{-0.71}$ scaling when plotting the measured diffusion coefficients against the molecular weights of monomeric eYFP and the protein complexes discussed above (likely stoichiometries were estimated based on current biophysical models of the cytosolic injectisome protein complexes) **(Fig. 5b**) (20, 34). This analysis allows us to distinguish between oligomerization models that differ in terms of protein complex stoichiometry. For example, earlier studies suggested that SctK, Q, Q_C, L, and possibly N, form a high molecular weight (>1MDa) complex, termed the sorting platform, that sequentially interacts with different secretion substrates and their chaperones(49, 50). However, efforts aimed at reconstituting sorting platform complexes *in vitro* have not been reported. The analysis in Figure 5b suggests that the majority of cytosolic injectisome proteins exist as part of smaller complexes with molecular weights of less than 500 kDa. Our combined results thus narrow down the possible stoichiometries of cytosolic injectisome protein complexes that can form prior to injectisome binding. Future work will need to determine the molecular structures of the complexes identified here and how their individual abundances change in response to environmental signals that induce T3SS assembly and activate secretion. However, as shown in this study, careful attention must be paid to the effect of the osmotic environment on cytosolic protein diffusion rates. Such efforts will help determine how the cytosolic injectisome proteins interact in the cytosol and when bound to injectisomes and how their dynamic exchange at injectisomes contributes to functional regulation of secretion.

MATERIALS AND METHODS

Bacterial Strains

Yersinia enterocolitica strains expressing fluorescent fusion proteins were generated by allelic exchange as previously described (39, 51). Mutator plasmids containing 250-500bp flanking regions, the coding sequence for eYFP, and a 13 amino acid flexible linker region between the fluorescent and target protein were introduced into *E. coli* SM10 λpir for conjugation with *Y. enterocolitica* pIML421asd. After sucrose counter-selection for the second allelic exchange event, colonies were grown overnight in BHI media (Sigma Aldrich, St. Louis, Missouri) with nalidixic acid (Sigma Aldrich) [35 µg/mL] and 2,6-diaminopimelic acid (Chem Impex International, Wood Dale, Illinois) [80 µg/mL]. PCR screening was then performed to confirm target insertion and constructs were confirmed by sequencing (GeneWiz, South Plainfield, New Jersey).

Cell Culture

Yersinia enterocolitica strains were inoculated from freezer stock one day prior to imaging and grown overnight in BHI media containing nalidixic acid (NaI) [35 µg/mL] and 2,6-diaminopimelic acid (dap) [80 µg/mL] at 28°C with shaking. On the day of imaging, 250 µL of overnight culture were transferred into fresh BHI media containing NaI, and dap and grown at 28°C with shaking for one hour. Glycerol [4 mg/mL], $MgCl_2$ [20 mM] and EDTA [5 mM] were then added to culture medium and transferred to a 37°C water bath with shaking for 3 hours to induce expression of the *yop* regulon and ensure secretion activation, respectively. Cells were pelleted by centrifugation at 5000x g for 3 minutes and resuspended three times into fresh M2G (4.9 mM Na_2HPO_4, 3.1 mM KH_2PO_4, 7.5 mM NH_4Cl, 0.5 mM $MgSO_4$, 10 µM $FeSO_4$ (EDTA chelate; Sigma), 0.5 mM $CaCl_2$) with 0.2% glucose as the sole carbon source. After the three washes, the remaining pellet was re-suspended in M2G, dap, $MgCl_2$, glycerol, and EDTA/$CaCl_2$. Cells were finally plated on 1.5 – 2% agarose pads in M2G containing dap, glycerol, and $MgCl_2$.

Secretion assay and protein analysis

Cultures were inoculated to an optical density at 600 nm of 0.12 from stationary overnight cultures. After 1.5 h of growth at 28°C, induction of the *yop* regulon was performed by shifting the culture to 37°C. Cultures were further incubated at 37°C for 3 hours. Bacteria from 2 ml culture were collected (15,000 g, 10 min, 4°C). 1.8 ml of supernatant was mixed with 0.2 ml trichloroacetic acid (final concentration 10%) and incubated over night at 4°C to precipitate proteins within the supernatant. Proteins were collected (15,000 g, 15 min, 4°C) and washed twice with ice-cold acetone (15,000 g, 5 min, 4°C). The pellet was dried at room temperature for 1 h. The pellet was resuspended in SDS-PAGE loading buffer (SDS (2% w/v), Tris-HCl (0.1 M), glycerol (10% w/v), DTT (0.05 M), pH = 6.8) and 0.6 OD units (1 OD unit is the equivalent of 1 ml culture at an OD_{600} of 1) in 15 µl were used for the SDS-PAGE gel analysis. For Western Blot analysis of the total cellular sample, the collected bacterial pellet was prepared for Western blot analysis by directly normalizing to 0.3 OD units in 15 µl loading buffer. All samples were heated for 10 min at 99°C before loading. Proteins were separated by SDS-PAGE on 15% acrylamide gels. For visualization, the gels were stained with InstantBlue (Expedeon). For immunoblots, the proteins were blotted on a nitrocellulose membrane. Detection of the eYFP-tag was performed by using primary rabbit antibodies against GFP (1:5000) (Invitrogen A6455, lot #1853896) and secondary anti-rabbit antibodies conjugated with horseradish peroxidase (1:10,000) (Sigma A8275). The immunoblot was visualized using ECL chemiluminescence substrate (Pierce) on a LAS-4000 Luminescence Image Analyzer (Fujifilm).

Single-Molecule Super-Resolution Fluorescence Imaging

Image data were acquired on a custom-built inverted fluorescence microscope based on the RM21 platform (Mad City Labs, Inc, Madison, Wisconsin), as previously described (18, 28). Immersion oil was placed between the objective lens (UPLSAPO 100 1.4 NA) and the glass cover slip (VWR, Radnor, Pennsylvania, #1.5, 22 mm 22 mm). Single-molecule images were obtained by utilizing eYFP photoblinking(52). A 514 nm laser (Coherent, Santa Clara, California, Genesis MX514 MTM) was used for excitation of eYFP (B350 W cm2). Zero order quarter wave plates (Thorlabs, Newton, New Jersey,

WPQ05M-405, WPQ05M-514, WPQ05M-561) were used to circularly polarize all excitation lasers, and the spectral profile of the 514 nm laser was filtered using a bandpass filter (Chroma, Bellows Falls, Vermont, ET510/10 bp). Fluorescence emission from both eYFP was passed through a shared filter set (Semrock, Rochester, New York, LP02-514RU-25, Semrock NF03-561E-25, and Chroma ET700SP-2P8). The emission path contains a wavelength specific dielectric phase mask (Double Helix, LLC, Boulder, Colorado) that is placed in the Fourier plane of the microscope to generate a double-helix point-spread-function(53, 54) (DHPSF). The fluorescence signals is detected on a sCMOS cameras (Hamamatsu, Bridgewater, New Jersey, ORCA-Flash 4.0 V2). Up to 20 000 frames are collected per field-of-view with an exposure time of 25 ms. A flip-mirror in the emission pathway enables toggling the microscope between fluorescence imaging and phase contrast imaging modes without having to change the objective lens of the microscope.

Data Processing

All fluorescence images were processed in MatLab using a modified version of the easyDHPSF code (18, 28, 55). To extract 3D localizations, fluorescence intensity from single-molecule emitters was fit to a double-Gaussian PSF model with maximum likelihood estimation. A median filter with a time window of 10 frames was used for background subtraction.

For each field-of-view, cell outlines were generated based on the phase contrast images using the open-source software OUFTI (56). Single-molecule localizations were then overlayed and aligned with the cell outlines. To ensure that single-molecule localizations align well with the corresponding cell, the cell outlines are registered to the fluorescence data by a two-step 2D affine transformation using the 'cp2tform' function in MATLAB. Five control points were manually selected based on the position of the cell poles of single-molecule localization data, which generated an initial transformation that allow for the removal of any cell containing less than 10 localizations. The center of mass for all the remining cells were then used to create a second, larger set of control pairs to compute the final transformation function. Only localizations within cell outlines were considered for further analysis.

Single-molecule Tracking Analysis

3D single-molecule localizations were filtered (**Supplementary Figure 2**) and linked into trajectories with a distance threshold of less than 2.5 µm between subsequent localizations. If two or more localizations were present in the cell at the same time, the trajectory was not considered for further analysis to prevent the incorporation of two or more molecules into the same trajectory. Any trajectories containing less than 4 localizations were also not considered for further analysis.

Trajectory information was then used to calculate the Mean Square Displacement (MSD)

$$MSD = \frac{1}{N}\sum_{n=2}^{N}\left(x_n - x_{n-1}\right)^2$$

where N is the total number of time points and x_n is the 3D position of the molecule at time point n. The apparent diffusion coefficient, D^*, of a given molecule trajectory was then computed as

$$D^* = \frac{MSD}{2 \cdot m \cdot \Delta t}$$

where $m=3$ is the dimensionality of the data and Δt is the camera exposure time. Δt=25 ms for all experiments reported here.

Monte Carlo Simulations

To resolve the unconfined diffusion coefficients of distinct molecular complexes in living cells based on the experimentally measured distribution of apparent diffusion coefficients, we simulated confined Brownian motion trajectories inside a cylindrical volume (radius = 0.4 μm, length = 5 μm). We added to our existing pool (28) of simulated diffusion coefficients to improve data fitting (see next section). Noisy, motion-blurred single-molecule images mimicking the raw experimental data were simulated for confined (in the cylindrical volume) single-molecules with defined Brownian diffusion coefficients. These images were then processed and linked into trajectories in the same manner as our experimental data. The resulting simulated CDFs account for confinement effects of the bacterial cell volume, signal integration over the camera exposure time, and experimentally calibrated signal-to-noise levels. Analyzing the simulation data

in the same manner as experimental data ensures that static and dynamic localization errors (28) are accurately modeled for our data fitting routine.

Data Fitting

Experimental distributions of apparent diffusion coefficients were fit using a linear combination of simulated CDFs, where each CDF corresponds to a single diffusive state described by a single diffusion coefficient. The coefficients of the best fitting linear combination were determined using the Matlab function lsqlin() with the trust-region-reflective algorithm (The MathWorks, Inc, Natick, MA). The resulting linear coefficients can be displayed as a spectrum of diffusion coefficients that manifest for a tracked protein in living cells. To establish the robustness of individual peaks in the diffusion coefficient spectrum, we resampled the raw data using bootstrapping (N = 100). We then average these bootstrapped spectra and used the resulting linear coefficients to fit the experimental data (mean bootstrapped spectrum fit). The mean bootstrapped spectrum provides us with an initial estimate of the diffusion coefficients of prominent diffusive states and their relative population fractions, estimated by determining the peak maxima and the area under the spectral peaks, respectively. The so-obtained parameters are then used as input parameters for non-linear fitting using the particleswarm() function in MATLAB. This approach allowed us to estimate the diffusion coefficients and population fractions of distinct diffusive states that manifest in living cells. In the case where the spectrum contains overlapping peaks or feature-less non-zero spectral density, we choose one or multiple diffusive states to initialize the non-linear fitting process. This approach results in the *n*-state (n = 1-4) fitting models shown in Supplementary Figs. 3-10, which are then evaluated using 5-fold cross-validation and qualitative agreement with the diffusion coefficient spectrum obtained by linear fitting.

References

1. Deng W, Marshall NC, Rowland JL, McCoy JM, Worrall LJ, Santos AS, Strynadka NCJ, Finlay BB. 2017. Assembly, structure, function and regulation of type III secretion systems. Nat Rev Microbiol 15:323–337.

2. Diepold A. 2020. Assembly and Post-assembly Turnover and Dynamics in the Type III Secretion System, p. 35–66. *In* Wagner, S, Galan, JE (eds.), Bacterial Type III Protein Secretion Systems. Springer International Publishing, Cham.

3. Diepold A, Armitage JP. 2015. Type III secretion systems: the bacterial flagellum and the injectisome. Philos Trans R Soc B Biol Sci 370:20150020.

4. Burkinshaw BJ, Strynadka NCJ. 2014. Assembly and structure of the T3SS. Biochim Biophys Acta BBA - Mol Cell Res 1843:1649–1663.

5. Wagner S, Grin I, Malmsheimer S, Singh N, Torres-Vargas CE, Westerhausen S. 2018. Bacterial type III secretion systems: a complex device for the delivery of bacterial effector proteins into eukaryotic host cells. FEMS Microbiol Lett 365.

6. Lara-Tejero M, Galán JE. 2019. The Injectisome, a Complex Nanomachine for Protein Injection into Mammalian Cells. EcoSal Plus 8.

7. Galán JE, Wolf-Watz H. 2006. Protein delivery into eukaryotic cells by type III secretion machines. 7119. Nature 444:567–573.

8. Type III Protein Secretion Systems in Bacterial Pathogens of Animals and Plants | Microbiology and Molecular Biology Reviews. https://journals.asm.org/doi/full/10.1128/MMBR.62.2.379-433.1998. Retrieved 15 February 2022.

9. Hu B, Lara-Tejero M, Kong Q, Galán JE, Liu J. 2017. In Situ Molecular Architecture of the Salmonella Type III Secretion Machine. Cell 168:1065-1074.e10.

10. Hu B, Morado DR, Margolin W, Rohde JR, Arizmendi O, Picking WL, Picking WD, Liu J. 2015. Visualization of the type III secretion sorting platform of Shigella flexneri. Proc Natl Acad Sci 112:1047–1052.

11. Kawamoto A, Morimoto YV, Miyata T, Minamino T, Hughes KT, Kato T, Namba K. 2013. Common and distinct structural features of Salmonella injectisome and flagellar basal body. 1. Sci Rep 3:3369.

12. Nans A, Kudryashev M, Saibil HR, Hayward RD. 2015. Structure of a bacterial type III secretion system in contact with a host membrane in situ. 1. Nat Commun 6:10114.

13. Butan C, Lara-Tejero M, Li W, Liu J, Galán JE. 2019. High-resolution view of the type III secretion export apparatus in situ reveals membrane remodeling and a secretion pathway. Proc Natl Acad Sci 116:24786–24795.

14. Oikonomou CM, Jensen GJ. 2019. Electron cryo-tomography of bacterial secretion systems. Microbiol Spectr 7:10.1128/microbiolspec.PSIB-0019–2018.

15. Berger C, Ravelli RBG, López-Iglesias C, Kudryashev M, Diepold A, Peters PJ. 2021. Structure of the Yersinia injectisome in intracellular host cell phagosomes revealed by cryo FIB electron tomography. J Struct Biol 213:107701.

16. Diepold A, Kudryashev M, Delalez NJ, Berry RM, Armitage JP. 2015. Composition, Formation, and Regulation of the Cytosolic C-ring, a Dynamic Component of the Type III Secretion Injectisome. PLOS Biol 13:e1002039.

17. Diepold A, Sezgin E, Huseyin M, Mortimer T, Eggeling C, Armitage JP. 2017. A dynamic and adaptive network of cytosolic interactions governs protein export by the T3SS injectisome. Nat Commun 8:1–12.

18. Rocha JM, Richardson CJ, Zhang M, Darch CM, Cai E, Diepold A, Gahlmann A. 2018. Single-molecule tracking in live Yersinia enterocolitica reveals distinct cytosolic complexes of injectisome subunits. Integr Biol 10:502–515.

19. Bernal I, Börnicke J, Heidemann J, Svergun D, Horstmann JA, Erhardt M, Tuukkanen A, Uetrecht C, Kolbe M. 2019. Molecular Organization of Soluble Type III Secretion System Sorting Platform Complexes. J Mol Biol 431:3787–3803.

20. Tachiyama S, Skaar R, Chang Y, Carroll BL, Muthuramalingam M, Whittier SK, Barta ML, Picking WL, Liu J, Picking WD. 2021. Composition and Biophysical Properties of the Sorting Platform Pods in the Shigella Type III Secretion System. Front Cell Infect Microbiol 11:488.

21. Brubaker RR, Surgalla MJ. 1964. The Effect of Ca^{++} and Mg^{++} on Lysis, Growth, and Production of Virulence Antigens by Pasteurella pestis. J Infect Dis 114:13–25.

22. Straley SC, Bowmer WS. 1986. Virulence genes regulated at the transcriptional level by Ca2+ in Yersinia pestis include structural genes for outer membrane proteins. Infect Immun 51:445–454.

23. Michiels T, Wattiau P, Brasseur R, Ruysschaert JM, Cornelis G. 1990. Secretion of Yop proteins by Yersiniae. Infect Immun 58:2840–2849.

24. Straley SC, Plano GV, Skrzypek E, Haddix PL, Fields KA. 1993. Regulation by Ca2+ in the Yersinia low-Ca2+ response. Mol Microbiol 8:1005–1010.

25. Pettersson J, Nordfelth R, Dubinina E, Bergman T, Gustafsson M, Magnusson KE, Wolf-Watz H. 1996. Modulation of Virulence Factor Expression by Pathogen Target Cell Contact. Science 273:1231–1233.

26. Karslake JD, Donarski ED, Shelby SA, Demey LM, DiRita VJ, Veatch SL, Biteen JS. 2021. SMAUG: Analyzing single-molecule tracks with nonparametric Bayesian statistics. Methods 193:16–26.

27. Elf J, Barkefors I. 2019. Single-Molecule Kinetics in Living Cells. Annu Rev Biochem 88:635–659.

28. Rocha J, Corbitt J, Yan T, Richardson C, Gahlmann A. 2019. Resolving Cytosolic Diffusive States in Bacteria by Single-Molecule Tracking. Biophys J 116:1970–1983.

29. Mika JT, Van Den Bogaart G, Veenhoff L, Krasnikov V, Poolman B. 2010. Molecular sieving properties of the cytoplasm of Escherichia coli and consequences of osmotic stress. Mol Microbiol 77:200–207.

30. Mika JT, Schavemaker PE, Krasnikov V, Poolman B. 2014. Impact of osmotic stress on protein diffusion in Lactococcus lactis. Mol Microbiol 94:857–870.

31. Minamino T, Macnab RM. 2000. FliH, a soluble component of the type III flagellar export apparatus of Salmonella, forms a complex with FliI and inhibits its ATPase activity. Mol Microbiol 37:1494–1503.

32. González-Pedrajo B, Fraser GM, Minamino T, Macnab RM. 2002. Molecular dissection of Salmonella FliH, a regulator of the ATPase FliI and the type III flagellar protein export pathway. Mol Microbiol 45:967–982.

33. Blaylock B, Riordan KE, Missiakas DM, Schneewind O. 2006. Characterization of the Yersinia enterocolitica Type III Secretion ATPase YscN and Its Regulator, YscL. J Bacteriol 188:3525–3534.

34. Bernal I, Römermann J, Flacht L, Lunelli M, Uetrecht C, Kolbe M. 2019. Structural analysis of ligand-bound states of the Salmonella type III secretion system ATPase InvC. Protein Sci Publ Protein Soc 28:1888–1901.

35. Okabe M, Minamino T, Imada K, Namba K, Kihara M. 2009. Role of the N-terminal domain of FliI ATPase in bacterial flagellar protein export. FEBS Lett 583:743–748.

36. Bai F, Morimoto YV, Yoshimura SDJ, Hara N, Kami-ike N, Namba K, Minamino T. 2014. Assembly dynamics and the roles of FliI ATPase of the bacterial flagellar export apparatus. Sci Rep 4:6528.

37. Imada K, Minamino T, Uchida Y, Kinoshita M, Namba K. 2016. Insight into the flagella type III export revealed by the complex structure of the type III ATPase and its regulator. Proc Natl Acad Sci U S A 113:3633–3638.

38. Case HB, Dickenson NE. 2018. MxiN Differentially Regulates Monomeric and Oligomeric Species of the Shigella Type Three Secretion System ATPase Spa47. Biochemistry 57:2266–2277.

39. Diepold A, Amstutz M, Abel S, Sorg I, Jenal U, Cornelis GR. 2010. Deciphering the assembly of the Yersinia type III secretion injectisome. EMBO J 29:1928–1940.

40. Muthuramalingam M, Whittier SK, Lovell S, Battaile KP, Tachiyama S, Johnson DK, Picking WL, Picking WD. 2020. The Structures of SctK and SctD from Pseudomonas aeruginosa Reveal the Interface of the Type III Secretion System Basal Body and Sorting Platform. J Mol Biol 432:166693.

41. Kinoshita M, Namba K, Minamino T. 2021. A positive charge region of Salmonella FliI is required for ATPase formation and efficient flagellar protein export. 1. Commun Biol 4:1–14.

42. Chen S, Beeby M, Murphy GE, Leadbetter JR, Hendrixson DR, Briegel A, Li Z, Shi J, Tocheva EI, Müller A, Dobro MJ, Jensen GJ. 2011. Structural diversity of bacterial flagellar motors. EMBO J 30:2972–2981.

43. McDowell MA, Marcoux J, McVicker G, Johnson S, Fong YH, Stevens R, Bowman LAH, Degiacomi MT, Yan J, Wise A, Friede ME, Benesch JLP, Deane JE, Tang CM, Robinson CV, Lea SM. 2016. Characterisation of Shigella Spa33 and Thermotoga FliM/N reveals a new model for C-ring assembly in T3SS. Mol Microbiol 99:749–766.

44. Wimmi S, Balinovic A, Jeckel H, Selinger L, Lampaki D, Eisemann E, Meuskens I, Linke D, Drescher K, Endesfelder U, Diepold A. 2021. Dynamic relocalization of cytosolic type III secretion system components prevents premature protein secretion at low external pH. Nat Commun 12:1625.

45. Mika JT, Poolman B. 2011. Macromolecule diffusion and confinement in prokaryotic cells. Curr Opin Biotechnol 22:117–126.

46. Stracy M, Schweizer J, Sherratt DJ, Kapanidis AN, Uphoff S, Lesterlin C. 2021. Transient non-specific DNA binding dominates the target search of bacterial DNA-binding proteins. Mol Cell 81:1499-1514.e6.

47. Bellotto N, Agudo-Canalejo J, Colin R, Golestanian R, Malengo G, Sourjik V. 2022. Dependence of diffusion in Escherichia coli cytoplasm on protein size, environmental conditions and cell growth. bioRxiv https://doi.org/10.1101/2022.02.17.480843.

48. Śmigiel WM, Mantovanelli L, Linnik DS, Punter M, Silberberg J, Xiang L, Xu K, Poolman B. 2022. Protein diffusion in Escherichia coli cytoplasm scales with the mass of the complexes and is location dependent. Sci Adv 8:eabo5387.

49. Lara-Tejero M, Kato J, Wagner S, Liu X, Galán JE. 2011. A sorting platform determines the order of protein secretion in bacterial type III systems. Science 331:1188–1191.

50. Johnson S, Blocker A. 2008. Characterization of soluble complexes of the Shigella flexneri type III secretion system ATPase. FEMS Microbiol Lett 286:274–278.

51. Kaniga K, Delor I, Cornelis GR. 1991. A wide-host-range suicide vector for improving reverse genetics in Gram-negative bacteria: inactivation of the blaA gene of Yersinia enterocolitica. Gene 109:137–141.

52. Biteen JS, Thompson MA, Tselentis NK, Bowman GR, Shapiro L, Moerner WE. 2008. Super-resolution imaging in live Caulobacter crescentus cells using photoswitchable EYFP. 11. Nat Methods 5:947–949.

53. Thompson MA, Lew MD, Badieirostami M, Moerner WE. 2010. Localizing and Tracking Single Nanoscale Emitters in Three Dimensions with High Spatiotemporal Resolution Using a Double-Helix Point Spread Function. Nano Lett 10:211–218.

54. Pavani SRP, Thompson MA, Biteen JS, Lord SJ, Liu N, Twieg RJ, Piestun R, Moerner WE. 2009. Three-dimensional, single-molecule fluorescence imaging beyond the diffraction limit by using a double-helix point spread function. Proc Natl Acad Sci 106:2995–2999.

55. Lew M, Lew* MD, von Diezmann* ARS, Moerner WE. 2013. Easy-DHPSF open-source software for three-dimensional localization of single molecules with precision beyond the optical diffraction limit. Protoc Exch https://doi.org/10.1038/protex.2013.026.

56. Paintdakhi A, Parry B, Campos M, Irnov I, Elf J, Surovtsev I, Jacobs-Wagner C. 2016. Oufti: an integrated software package for high-accuracy, high-throughput quantitative microscopy analysis. Mol Microbiol 99:767–777.